2021

Constructing a Rainbow OLED Using Fabry-Pérot Microcavities

Alex Howe
University of Vermont

Constructing a Rainbow OLED Using Fabry-Pérot Microcavities

Alex Howe

University of Vermont
Department of Physics

Spring 2021
Defended on May 6, 2021

Abstract

The objective of this project is the creation of microcavity-based organic light-emitting diodes (OLEDs) emitting light across the visible spectrum, building on Ben Isenhart's findings on the control of OLED devices' peak emission and Gather et al's work with multicolored OLEDs. Both theoretical and experimental work is pursued for this project. Device fabrication is experimentally challenging and required thin film deposition without substrate rotation to deposit charge transport layers with a linear gradient. The emission spectrum of fabricated devices is characterized using angle-resolved electroluminescence spectroscopy (ARES). While the simulated devices show emission across the visible spectrum from red-orange to blue-violet, the fabricated devices only emitted light in the blue to green range. The findings do confirm that varying cavity thickness does alter the emission spectrum of a device. In order to create a device with emission spanning more of the visible spectrum, there are multiple experimental methods that can be used to achieve more variation in device thickness across either one device or a batch of devices.

Contents

Chapter 1

Introduction

1.1 Organic Light-Emitting Diodes (OLEDs)

Organic light-emitting diodes (OLEDs) are derived from LEDs, which use semiconducting materials to generate light. OLEDs employ organic semiconductors for this purpose to avoid the environmental hazards associated with semiconductors commonly used in LEDs, such as gallium arsenide [1]. OLEDs are promising for applications in display technology.

The simplest possible OLED would consist of one layer of organic material between a metal cathode and an transparent conducting oxide anode such as indium tin oxide (ITO). The application of an electric field causes holes to be injected from the anode and to move across the highest occupied molecular orbitals (HOMO); from the cathode, electrons move in the opposite direction and across the lowest occupied molecular orbitals (LUMO) [2]. Recombination occurs at a specific zone inside the organic later, which forms excitons [2]. The formed excitons then relax into their ground states and produce photons, which are then reflected from the cathode or pass directly through the anode [2]. This process of hole-electron recombination, called electroluminescence, is the basis for how OLEDs emit light via spontaneous emission [3]. It is also possible to create top- or bottom-emitting OLEDs by making one electrode transparent and the other reflective so that photons are emitted through the transparent cathode; top-emitting OLEDs are often used so that films can be deposited onto inexpensive substrates [2].

Recently, research has focused on p-i-n type OLEDs [2]. Using this architecture, OLED optical media have at least three main layers: a hole transport

layer (HTL), where positive charges travel from the anode to the recombination zone; an electron transport layer (ETL), where electrons travel from the cathode to the recombination zone; and the emissive layer (EML), sandwiched between the HTL and ETL, where recombination occurs [2, 4, 5]. The ETL and HTL are formed by n- and p-type semiconducting materials, respectively. Additionally, charge injection layers of approximately one nanometer in thickness can be added adjacent to the electrodes to improve electrical contact of the metal and to avoid damage to the device[2]. For instance, Matsushima et al. found that using a 0.75 nm-thick layer of molybdenum(VI) oxide (MoO_3) as a hole injection layer (HIL) reduced the driving voltage and improved power efficiency [6].

P-i-n-type OLEDs prove useful due to their lower operating voltages and higher power efficiency [2]. Moreover, OLEDs utilizing a p-i-n structure have longer lifetimes (defined by the time it takes for luminance to drop to one-half of its initial value) and involve fewer outcoupling losses under operation [2]. However, the lifetime of an OLED operated with a surface luminance of at least 30000 cd/m^2 (the amount required for lighting) decreases as as the operating temperature rises [7].

1.2 Fabry-Pérot microcavities

Fabry-Pérot microcavities are desirable for use in OLEDs because they narrow the emission spectra from the microcavity effect [8, 9]. While more traditional OLEDs incorporate a transparent anode (such as ITO), employing a microcavity architecture by manufacturing the anode from a partially reflective and partially transmissive material further narrows the emission spectra to allow only resonant modes in the form of standing waves as a result of exciton-photon coupling [5, 10]. It is also possible to create a Fabry-Pérot OELD using a dielectric mirror [5]. Peak photoluminescence (light emission) of a cavity corresponds to the intensity of light, which must coincide with the resonant wavelength [3]. An advantage of using a Fabry-Pérot microcavity architecture for an OLED is that the intensity of the peak wavelength is dramatically enhanced [11].

There are multiple ways to modify the resonant wavelength, and consequently the emission spectra, of an OLED. Modifying the chemical composition of the optical media, such as with dopants, modifies the microcavity's properties by altering the resonant wavelength [12]. Furthermore, higher-

order resonance modes (such as the λ or $\frac{3}{2}\lambda$ modes) involve a narrower bandwidth of emission peaks. Varying the cavity's thickness changes the resonant modes and thus alters the peak wavelength; this is because peak emission is determined by optical path length [11]. However, increasing the thickness of cavity layers requires a higher operating voltage to produce the same current density during operation. More specifically, the relationship between the peak wavelength of one mode and optical path length is given by

$$j\frac{\lambda_j}{2} = nd\cos\theta, \tag{1.1}$$

where j (an integer greater than 0), represents a mode, λ_j is the peak wavelength of the j^{th} mode, nd is the optical path length of the organic layers, and θ is the viewing angle [5].

The transmission coefficient of light in a Fabry-Pérot microcavity as a function of phase shift between forward- and backward-propagating waves inside the cavity (ϕ) is given by

$$T(\phi) = \frac{I_{trans}}{I_{inc}} = \frac{(1-R_1)(1-R_2)}{(1-\sqrt{R_1R_2})^2 + 4\sin^2\phi\sqrt{R_1R_2}}, \tag{1.2}$$

in which R_1 and R_2 are the reflectivities of the top and bottom electrodes. Phase shift is specified by the expression

$$\phi = \frac{2\pi nd}{\lambda}, \tag{1.3}$$

but since the phase shift must be an integer multiple of phi from resonance conditions, $\sin\phi = 0$, and thus

$$T(\phi) = \frac{(1-R_1)(1-R_2)}{(1-\sqrt{R_1R_2})^2}[5]. \tag{1.4}$$

The forward emission spectrum can be calculated by the equation

$$|E(\lambda)|^2 = \frac{(1-R_1)(1+R_2+2\cos(\frac{4\pi x}{\lambda})\sqrt{R_2})}{1+R_1R_2-2\cos(\frac{4\pi L}{\lambda})\sqrt{R_1R_2}}|E_f(\lambda)|^2, \tag{1.5}$$

where $E_f(\lambda)$ is the free-space emission spectrum of the EML, x is the effective distance between the EML and the top electrode, and L is the optical path length of the entire device [5].

For microcavity-based OLEDs with emission in the fundamental resonant mode ($j = 1$), the wavelength would be in the visible spectrum assuming that the device's optical medium has a thickness of approximately 100 nm and a refractive index between 1.5 and 2 [5]. However, multi-mode devices, which correspond to multiple emission peaks, can be created when multiple cavity modes overlap with the free space emission spectrum of the EML; higher-mode devices can be fabricated by increasing the optical path length [5, 11]. The intensities of multiple peaks correspond to the location of emitting dipoles (in essence, the thickness of the EML) [11].

The quality factor (Q), a measure of the narrowness of emission peaks, of a microcavity is given by the formula

$$Q = \frac{\lambda_0}{\delta\lambda}, \tag{1.6}$$

in which λ_0 represents the resonant wavelength and $\delta\lambda$ is the full width at half maximum (FWHM) of the emission peak [5]. The Fabry-Pérot microcavity's steady-state solution gives another expression for Q, based on energy dissipation, as

$$Q = j\frac{\pi(R_1R_2)^{\frac{1}{4}}}{1-\sqrt{R_1R_2}}, \tag{1.7}$$

demonstrating that higher-mode devices have higher quality factors [5].

1.3 ARES

ARES reveals that the intensity of emitted light in a resonant microcavity involves angular dependence due to the transmission across a material interface with a difference in in the refractive index; however, the radiation patterns observed at the peak wavelength involve the least variation with angle [13]. Additionally, the intensity and wavelength of emission are generally largest at normal emission, with possible exceptions due to mode overlap or dipole positions in the EML [5]. This relationship occurs since the spatial distribution of optical modes changes with angle from the cavity's boundary conditions [9]. In microcavity-based devices with high Q, the wavelength falls off even more rapidly with deviation from normal viewing angle [9].

Moreover, at high angles, the resonant mode splits into two peaks corresponding to the transverse electric (TE), or s-polarization, and transverse magnetic (TM) modes, or p-polarization [5]. The splitting of modes is caused

by phase shift of the light being reflected from the metal electrodes [14]. Additionally, at high angles, a deviation from the relationship in Eq. (1.1) occurs.

1.4 Color emissions

The color of emission perceived by the human eye can be characterized by the CIE's (Commission Internationale de l'Éclairage) 1931 colorimetry system, which is associated with a set of wavelength-specific color-matching functions. The color matching functions are integrated across the power spectrum with respect to wavelength, which produces tristimulus values that are plotted on a chromaticity curve. The chromaticity coordinates correspond to the color of emission [15]. Furthermore, the chromaticity curve according to the CIE 1931 standard represents the entire color gamut of the visible spectrum.

1.4.1 Work elsewhere

Traditionally, colored OLEDs were fabricated using dyes and dopants. For instance, Tsuzuki et al. demonstrated color tuning of OLEDs to green and yellow light using phosphorescent dyes [16].

Puzzo et al. were able to create mixed-color OLEDs from a device with three modes, one for each of the primary colors used in displays [4]. Doping the EML with dyes can also change the color of the emitted light; for instance, the team found that using pyrromethene 580 as a dopant enhanced the red portion of the emission spectrum [4]. Doping the HTL and ETL can also achieve similar color changes; in 2006, a highly efficient deep red OLED was fabricated using an HTL doped with NDN1 (a material produced by Novaled AG) and an ETL doped with cesium [2]. Due to the stability of the materials of the EML of red OLEDs, red OLEDs have longer lifetimes than blue and green OLEDs [2].

Efficient blue-emitting devices have been creating using additional layers known as charge blocking layers, which prevent the escape of holes and electrons after they enter the EML to raise recombination rates [2]. Furthermore, in 2015, Hellerich et al. constructed an OLED emitting deep blue wavelengths, notable because the blue and violent parts of the visible spectrum are difficult to emit due to their small wavelengths [17]. This was accomplished by creating an optical medium from mixed polymers [17].

Dodabalapur et al proposed in 1993 that tri-color devices could be created by taking advantage of the microcavity effect and altering the thickness of various layers [9]. Similarly, Liu et al in 2011 demonstrated that a multi-colored device could be created using varying thickness of MoO_3 as an HIL and an optical spacer [18].

In 2010, Ventsch et al. produced a microdisplay spanning a wide color range by incorporating red-, blue-, and green-emitting OLEDs as display subpixels. Ventsch et al. produced top- and bottom-emitting microcavity devices (using glass substrates with Ag and ITO anodes, respectively) and a complementary metal–oxide–semiconductor (CMOS)-compatible device (with a silicon substrate and Al and Ag electrodes). The red- and blue-emitting OLEDs achieved brightness levels of 1000 cd/m^2, and the green-emitting OLED's brightness level was 10000 cd/m^2, all at operating voltages below 7V [19]. The blue-emitting devices had the lowest efficiencies due to the broad emission spectrum of the blue emitter [19].

In 2015, Gather et al. constructed an OLED emitting discrete rainbow colors. A wedge was deposited beneath the HTL to create an optical media with a linearly increasing total thickness, accompanied by an EML of unchanging thickness. Multiple electrodes were placed on top of the optical media to create multiple different OLEDs with resonant wavelengths across the visible spectrum. This architecture is known as a frequency comb [20].

1.4.2 Work at UVM

Isenhart demonstrated that peak emission and bandwidth of a Fabry-Pérot-based OLED can be adjusted by simply increasing or decreasing device thickness without modifying the chemical contents of the layers. Changing resonant wavelength by altering cavity thickness would be preferable over making material modifications for experimentally convenience. Isenhart also found that, within each resonant mode, increasing cavity thickness causes a redshift in wavelength and that there is an approximately linear relationship between cavity thickness and emitted wavelength. Moreover, for higher order modes, the wavelength increased at a slower rate [10].

Moreover, in 2021, the Device Physics Research Group at the University of Vermont produced microcavity-based OLEDs emitting light spanning the entire visible spectrum while also achieving high quality factors [5]. Three devices with increasing thickness, corresponding to the $\frac{\lambda}{2}$, λ, and $\frac{3}{2}\lambda$ modes, were produced [5]. The devices each consisted of a silver (Ag) anode, a

MoO_3 HIL, an aluminum (Al) cathode, a lithium fluoride (LiF) electron injection layer (EIL), N,N'-Di(1-naphthyl)-N,N'-diphenyl-(1,1'-biphenyl)-4,4'-diamine (NPB) as the HTL, bathophenanthroline (BPhen) as the ETL, tris(8-hydroxyquinolinato)aluminum (Alq_3), a green emitter frequently used in multi-layer devices, as the EML, along with a silicon wafer substrate acting as a heat sink to allow for high power operation but differed in the combined thickness of the optical layers [5, 21].

Increasing cavity thickness resulted in wavelength emissions across the visible spectrum and the pumping of high-order resonance modes, demonstrating a linear relationship between peak wavelength and cavity thickness with a slope inversely proportional to the mode index j [10]. Notably, higher order modes exhibited narrower emission peaks [10]. ARES measurements revealed an angular dependence on emitted color, with blueshift of the peak wavelength occurring as the incident angle and order of the resonant mode increased [10]. Notably, the $\frac{3}{2}\lambda$ mode device emitted violet light at off-normal emission, with higher modes appearing at higher viewing angles [5].

1.5 Significance

Multi-colored OLEDs have promising applications for digital screens, lighting, spectroscopy, and for biological and chemical sensors. More specifically, the advantages that OLEDs have over liquid crystal displays (LCD) involve a lighter weight, high contrast, low operating voltage, a wider viewing angle, and reduced operation cost [2]. Optical microcavities are also promising for applications of quantum computing by allowing the transfer of quantum information between atoms and photons [22].

Furthermore, a rainbow OLED combines the features of a photonic crystal (such as an opal or similar crystal) with the characteristics of an optoelectronic device and therefore presents potential for multiple research interests. For instance, this device could be used to more effectively examine the coupling between the cavity resonator and emitter dipole; since the device thickness increases according to a linear gradient, all possible resonance overlap conditions can be tested, whereas some conditions may be missed if thickness increases in discrete steps. Moreover, part of my personal motivation for building a rainbow OLED is my status as an openly queer and transgender physics student.

Chapter 2

Methodology

Due to restrictions on laboratory access during the COVID-19 pandemic, a combination of theoretical and experimental work was pursued for this project.

The same device structure was used for both theoretical and experimental components (see Table 2.1 and Fig. 2.1 for layer thicknesses and device schematics). The OLED will be composed of a silicon wafer substrate, an anode of Ag, an HIL of MoO_3, a cathode of Al, and an EIL of LiF. Within the optical medium, the HTL is composed of NPB, the EML is made of Alq_3, and the ETL consists of 2,9-Dinaphthalen-2-yl-4,7-diphenyl-1,10-phenanthroline (NBPhen). NBPhen is useful as an ETL material since it is a derivative of the commonly used BPhen.

Ag and Al were used as electrodes due to their properties of conductivity and reflectivity. MoO_3 is useful as a material for the HIL due to its high conductivity and heat resistivity. While Alq_3 has a large spectral linewidth,

Material	Layer	Thickness (nm)
Ag	Anode	100
MoO_3	HIL	1
NPB	HTL	x
Alq_3	EML	10
NBPhen	ETL	x
LiF	EIL	1
Al	Cathode	30

Table 2.1: Thickness of device layers, where x is a variable thickness.

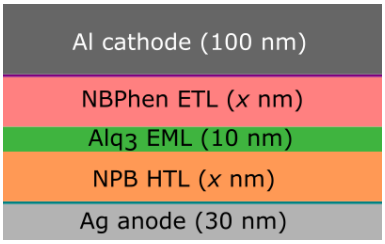

Figure 2.1: Device schematic with x denoting variable thickness. Not labelled are the EIL in violet (LiF, 1 nm) and HIL in teal (MoO_3, 1 nm).

narrowing of its bandwidth occurs due to the microcavity effect [9].

2.1 Simulation

Devices and emissions were simulated using a MATLAB program developed by the Device Physics Research Group. The program allows devices to be simulated by creating layers of materials with associated thicknesses, optical properties, and roughness. The structure program also specifies the dipole layer.

2.1.1 Devices

To simulate device gradients, a range of simulated devices according to the specifications above were created.The HTL and ETL thicknesses of the simulated devices ranged from 35 nm to 70 nm, yielding total optical media thicknesses from 80 nm to 150 nm.

2.1.2 Measurements

The OLED device's emission spectra must be calculated using the transfer matrix method, a computational method describing the interaction of electromagnetic waves with 2D planar structures based on Fresnel coefficients and the optical properties of layers to compute the incident, transmitted, and reflected waves on both sides of the microcavity. This method incorporates partial reflections, polarization, and allows for emissions at angles other than the normal [23].

Orientation	TE	TM
Horizontal	$A_{\uparrow,\downarrow} = \pm\sqrt{\frac{3}{16\pi}}$	$A_{\uparrow,\downarrow} = \pm\sqrt{\frac{3}{16\pi}}\cos\theta$
Vertical	$A_{\uparrow,\downarrow} = 0$	$A_{\uparrow,\downarrow} = \sqrt{\frac{3}{8\pi}}\sin\theta$

Table 2.2: Source terms from Benisty et al for horizontal and vertical dipoles and for TE and TM modes used in the simulation. Source terms are vectors with one component each for forward and backward propagation.

Within a layer j of the device, the electric field can be represented by a superposition of two electric fields travelling in opposite directions (see Fig. 2.2),

$$E_j = E_j^{\uparrow}\exp\left(i[k_j x - \omega t]\right) + E_j^{\downarrow}\exp\left(-i[k_j x + \omega t]\right), \tag{2.1}$$

in which $E_j^{\uparrow}$ and $E_j^{\downarrow}$ represent the magnitudes of the forward- and backward-propagating electric fields.

Utilizing the definition $q_j = \tilde{n}_j - (\tilde{n}_{ext}\sin\theta_{ext})^2$ (where n_{ext} and refer to the refractive index for air), the polarized Fresnel coefficients for the interface between adjacent layers j and k are

$$r_{j,k}^{s} = \frac{q_j - q_k}{q_j + q_k}, \tag{2.2}$$

$$r_{j,k}^{p} = \frac{\tilde{n}_k^2 q_j - \tilde{n}_j^2 q_k}{\tilde{n}_k^2 q_j + \tilde{n}_j^2 q_k}, \tag{2.3}$$

$$t_{j,k}^{p} = \frac{2\tilde{n}_k\tilde{n}_j q_j}{\tilde{n}_k^2 q_j + \tilde{n}_j^2 q_k}, \tag{2.4}$$

and

$$t_{j,k}^{s} = \frac{2q_j}{q_j + q_k}. \tag{2.5}$$

Here, s and p-polarization correspond to horizontal and vertical dipoles, respectively. From conservation of energy, the scattering matrix can be defined:

$$\boldsymbol{M_{j-1,j}} = \frac{1}{t_{j-1,j}}\begin{pmatrix} 1 & r_{j-1,j} \\ r_{j-1,j} & 1 \end{pmatrix}, \tag{2.6}$$

where the electric fields between layers $j-1$ and j are related according to

$$E_{j-1}^{\uparrow\downarrow} = \boldsymbol{M_{j-1,j}} E_j^{\uparrow\downarrow}. \tag{2.7}$$

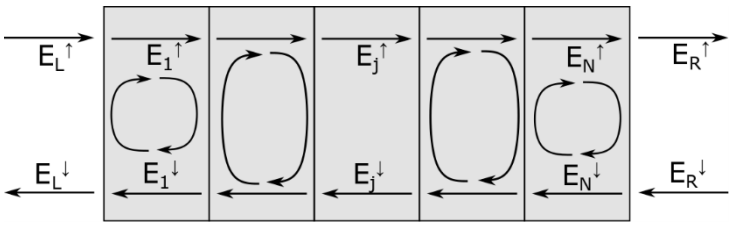

Figure 2.2: An illustration of electric waves inside each layer of a device.

Similarly, at the next interface between layers j and $j+1$, a propagation matrix is used to determine the magnitude of the electric field transmitted through layer j based on phase shift,

$$\boldsymbol{D_j} = \begin{pmatrix} \exp\left(ik_{z,j}d_j\right) & 0 \\ 0 & \exp\left(-ik_{z,j}d_j\right) \end{pmatrix}, \tag{2.8}$$

in which $k_{z,j}$ is the perpendicular component of the k vector in layer j and d_j is the thickness of layer j, meaning the electric fields to the left and right of layer j as

$$E_{j\uparrow}^{\uparrow\downarrow} = \boldsymbol{D_j} E_{j\downarrow}^{\uparrow\downarrow}. \tag{2.9}$$

In order to calculate the electric field at a point k across multiple layers from the electric field at point j, equations 2.6 and 2.9 are combined to form the transfer matrix,

$$\boldsymbol{S_{j\rightarrow k}} = \prod_{n=j}^{k} \boldsymbol{M_{j-1,j}} \boldsymbol{D_j}, \tag{2.10}$$

such that

$$E_j^{\uparrow\downarrow} = \boldsymbol{S_{j\rightarrow k}} E_k^{\uparrow\downarrow}. \tag{2.11}$$

To calculate emission spectra inside a microcavity, two transfer matrices (one each for the left- and right-hand sides of the stack) are calculated using the source terms given in Benisty et. al and outlined in Table 2.2, given by

$$E_L^{\uparrow} = \boldsymbol{S_{L\rightarrow k}} A_{s,p}^{\uparrow,\downarrow} \tag{2.12}$$

and

$$E_R^{\downarrow} = \left(\boldsymbol{S_{k\rightarrow R}}\right)^{-1} A_{s,p}^{\uparrow,\downarrow}. \tag{2.13}$$

This gives rise to a system of linear equations that can be solved for the electric fields on both sides,

$$\begin{pmatrix} 0 \\ E_L^{\downarrow} \end{pmatrix}^{(s,p)} = \boldsymbol{S_L} \begin{pmatrix} A^{\uparrow} \\ A^{\downarrow} \end{pmatrix}^{(s,p)} \tag{2.14}$$

and

$$\begin{pmatrix} E_R^{\uparrow} \\ 0 \end{pmatrix}^{(s,p)} = \boldsymbol{S_R} \begin{pmatrix} A^{\uparrow} \\ A^{\downarrow} \end{pmatrix}^{(s,p)} . \tag{2.15}$$

The program simulates all experimental observations, including the relationship between peak wavelength, bandwidth, and polarization and cavity thickness. The program applies an exciton profile to the dipole position, calculates power from the electric fields, and plots power as a function of wavelength and angle. The program also allows for specifying the ratio of horizontal to vertical dipoles, which is determined by molecular orientation inside the optical medium, with charge transport layers exhibiting horizontal orientation [24]. For the simulation, a 30:1 horizontal to vertical dipole ratio was used.

2.2 Experiment

2.2.1 Device fabrication

The primary experimental challenge of this project was the linear thermal evaporation of material for ETL and HTL. Measurements conducted on the linear depositions of aluminum and NPB reveal that the thicknesses change by approximately 30% and 50% (respectively) across one batch of ITO-coated substrates. Depositions were performed using substrates placed along the diagonal of a square substrate holder (see upper half of Fig. 2.3).

A layer of SiO_2 with a thickness on the order of 100 nm was grown on the silicon substrates. The same layers outlined in Table 2.1 were used, with additional layers of chromium contact pads and bars of 58 nm total thickness between the substrate and anode to allow the thin films to stick to the substrate. For the depositions of the two charge transport layers, the diagonal line of substrates was rotated to align with each of the two sources to maximize the linear gradient (see lower half of Fig. 2.3). For all materials but the ETL and HTL (the materials deposited with a constant thickness), the substrate rotated with a speed of 10 rpm.

The evaporation rates for were 0.3 Å/s for MoO_3, 0.1 Å/s for LiF, 1.5 Å/s for Al, 1.0 Å/s for Ag, and 0.5 Å/s for Alq_3, NPB, and NBPhen. All fabrication shall take place in a vacuum chamber with a pressure of 10^{-7} torr. Devices were handled and stored in a nitrogen chamber with < 0.1 ppm

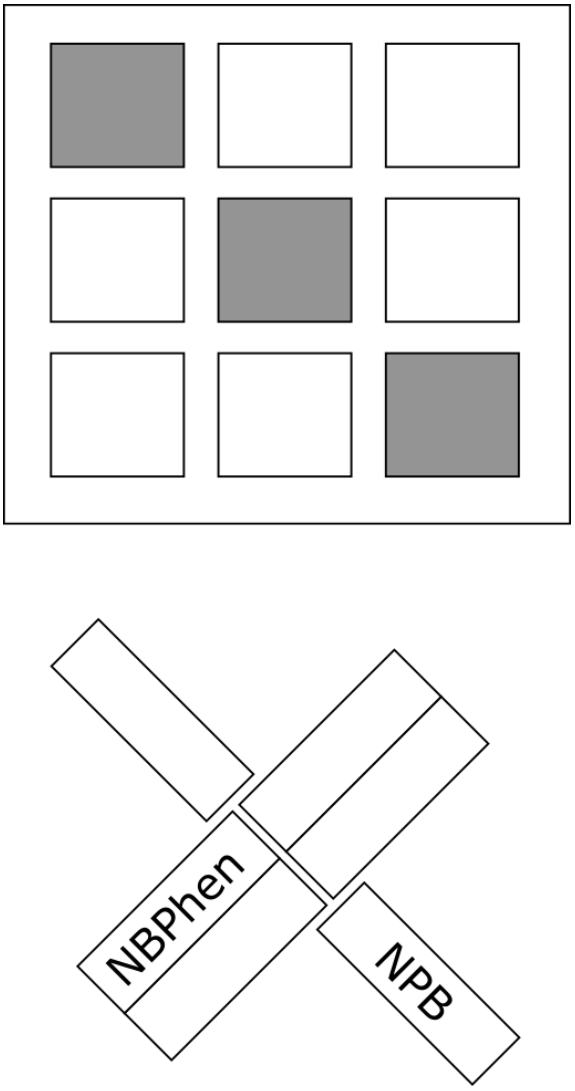

Figure 2.3: Above: the substrate holder. The grey squares show the location of the devices. The substrate holder rotates at a speed of 10 rpm for layers of constant thickness.
Below: location of sources beneath the substrate holder. Since each source is not centered below the holder, it is necessary to rotate the substrate holder for the deposition constant-thickness layers.

O_2 and < 0.5 ppm H_2O. All organic materials were purchased from Sigma-Aldrich, and the silver and aluminum were purchased from R.D. Mathis.

2.2.2 Measurements

ARES measurements were conducted using an Ocean Optics HDX spectrometer. Device emissions were passed through an iris to control collection angle and then reflected off of a parabolic mirror to focus the emission. The emitted wavelength is measured on an interval of 0 to 70 degrees with a step of no larger than 0.5 degrees, utilizing an automatically rotating stage programmed using LabView.

Chapter 3

Results

3.1 Simulation

The peak wavelengths ranged from 425 nm (3.1) to 630 nm (from the thinnest and thickest devices, respectively). Peak intensity occurred at high angles, with the thinnest at 58.5°and the thickest at 68.5°since the dipole position is located in the center of the device, which suppresses normal emission. The devices with charge transport layers of approximately 60 nm and thicker resulted in emission in both the $\frac{\lambda}{2}$ and λ modes, as shown in Fig. 3.2. Starting with the devices with charge transport layers of about 67 nm, the second mode decreased in intensity. The simulated emission spectra involve a band with less than background intensity near the emission band as a consequence of the simulation.

The results from one continuous device with gradient thickness were estimated by incorporating each device into a plot of peak wavelength as a function of distance along the device (3.3). Each device was treated as having a length of 1 mm, with the thinnest device at 0 mm and the thickest at 35 mm. Based on this method of incorporating the simulated devices, the peak wavelength ranges from 425 nm (blue) to 630 nm (orange). This relationship demonstrates that the peak wavelength increases linearly with the optical path length, as demonstrated by Eq. 1.1.

Using the CIE 1931 color-matching functions, the perceived color of the emission spectra of all theoretical devices at the angle producing the maximum intensity is described by Fig.3.4). The thinnest device produces blue-violet emission, and as the device thickness increases, the color shifts to blue,

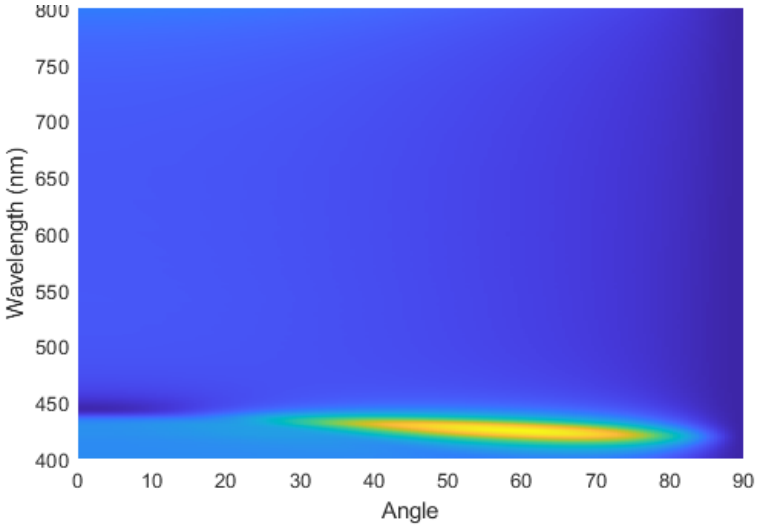

Figure 3.1: Emission from device with 35 nm-thick charge transport layers.

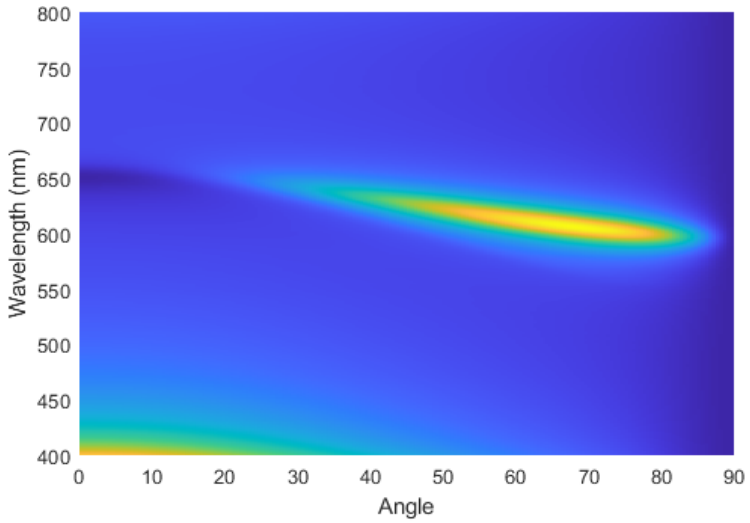

Figure 3.2: Emission in both the $\frac{\lambda}{2}$ and λ modes in device with an HTL and ETL thickness of 67 nm.

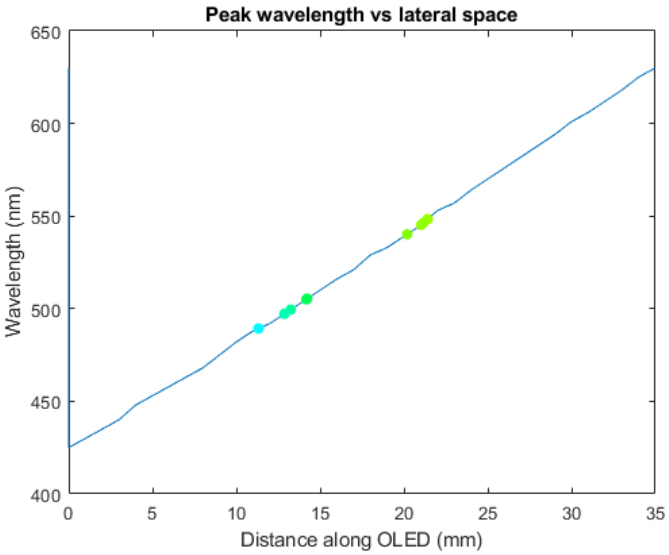

Figure 3.3: Plot of peak wavelength as a function of lateral distance along simulated gradient OLED. The slope represents the increase in optical path length from a 1-nm increase in the thicknesses of the charge transport layers. The green and blue data points represent the peak wavelengths of the fabricated devices.

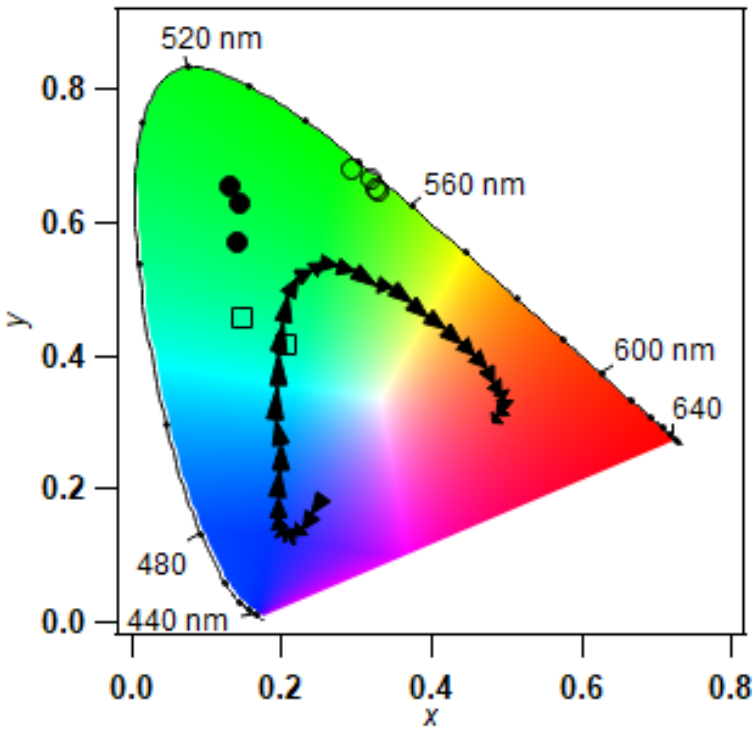

Figure 3.4: Chromaticity coordinates of devices. Theoretical devices are represented with the arrows; device thickness increases counter-clockwise along the curve. The hollow circles, filled circles, and hollow squares represent emissions from pixels of the $\approx$ 86 nm, $\approx$ 104 nm, and $\approx$ 138 nm devices, respectively

to green, to yellow, to orange, and the thickest device gives red-orange emission. Fig. 3.4 demonstrates that the emission of the theoretical devices at peak intensity spans the visible spectrum.

3.2 Experiment

Fig 3.5 shows the physical appearance of the thickest device after fabrication. Measurements were taken from all functioning pixels: four pixels on the thickest device (with pixels with optical media thicknesses of around 135 nm), three on the device with middle thickness (consisting of active layers of about 104 nm), and two from the thinnest device (corresponding to optical

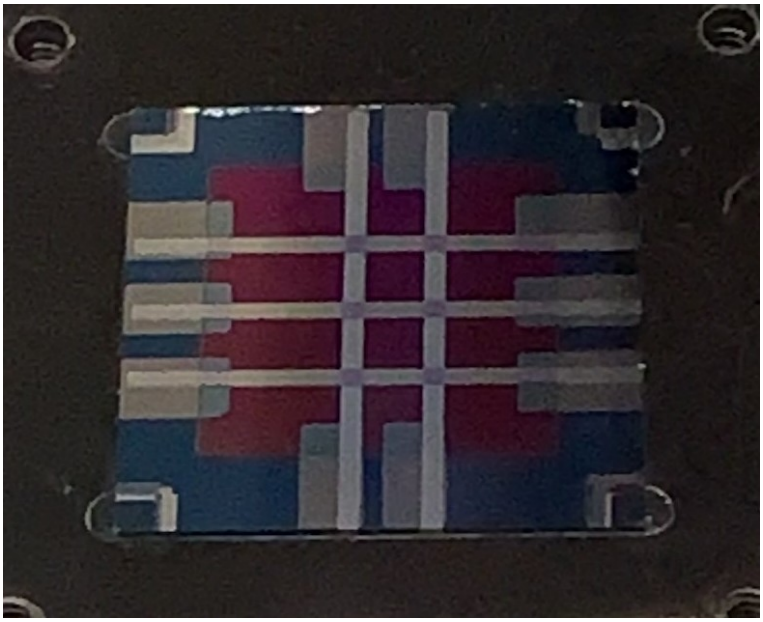

Figure 3.5: The thickest device produced in the experiment. The device's six pixels are the cross-section between the electrodes in the two- and three-bar patterns.

media thicknesses of around 85 nm).

3.2.1 Peak wavelength

All four pixels from the device with an average thickness of 135 nm produced lime-green colored emission, with subtle differences in peak wavelength between the four pixels. When operated at 8V and 2 mA, the pixel with 135 nm optical thickness emitted light at a peak wavelength of 548.4 nm. The pixel with an active layer about 133 nm thick produced a peak wavelength of 546.2 nm. pixel 5 exhibited peak emission at 545.2 nm, and pixel 6 produced peak emission at 545.2 and 540.2 nm, respectively.

Pixels on the device with the active layer thicknesses of about 104 nm were lit in a blue-green color, which appeared blue when observed at higher angles. The pixel with 104.5 nm medium thickness had peak emission at 505.1 nm, and the pixel with about 104 nm optical medium thickness produced a peak wavelength of 505.4 nm. The pixel of approximately 101 nm medium thickness emitted light at a peak wavelength of 499.5 nm when operated at 8V and 1 mA.

The two pixels on the device of about 86 nm thick organic layers were operated at 8V but driven at a higher current of 5 mA since operation at 2 mA yielded emission at a lower intensity. The color of this light was a pale blue. Crosstalk between the operated pixels and the pixels to the left took place, which somewhat compromises the ARES spectra of the devices. Pixels with medium thicknesses of 86 and 83 nm produced peak wavelengths of 497.2 and 489.3 nm, respectively.

The slight variations in peak wavelength between pixels (summarized in Table 3.1) are in line with the differences in thickness across the diagonal of each device. In comparison to the theoretical work, Fig 3.3 plots these observed peak wavelengths with a linear interpolation to estimate the position of each pixel across the simulated gradient device. The light blue pixel with the shortest peak wavelength would correspond to a lateral distance of about 11.3 mm, and the lime-green pixel corresponds to approximately 21.4 mm.

3.2.2 Angular emission patterns

Similarly to the peak wavelength, the wavelengths associated with the emission bands shift slightly between each pixel. For instance, the pixels with optical media thicknesses of about 135 and 133 nm optical thicknesses are

Appx. medium thickness (nm)	Peak wavelength (nm)
135	548.4
133	546.2
132	545.2
130	540.2
104.5	505.1
104	505.4
101	499.5
86	497.2
83	489.3

Table 3.1: Summary of peak wavelength and estimated thickness from each pixel.

located on the same substrate, but the ARES profile of the 133 nm-thick pixel (Fig 3.6b) involves slightly shorter wavelengths than (Fig 3.6a). The majority of the pixels also involve visible emission from 0 to approximately 40°.

With the exceptions of the 104.5 nm-thick (Fig 3.7a) and 489.3 nm-thick pixels (Fig 3.8b), all pixels show high-intensity normal emissions. This is a significant deviation from the theoretical predictions. A likely explanation for this is that the thickness of both the charge transport layers is slightly unequal in these devices, which would mean that the dipole emitter is not the center of the optical medium, thus allowing normal emission.

Notably, neither pixel from the device with 86 nm-thick organic layers (Figs. 3.8a and 3.8b) experiences the cavity effect's narrowing of emission; as a result, these emission patterns correspond to the free-space emission of Alq_3. Since these pixels correspond to the thinnest ETL and HTL, the resonant wavelength is likely too far in the ultraviolet part of the spectrum to be seen.

3.2.3 Emission color

The circles and squares on the curve in Fig 3.4 show the color of emission at peak angle. Although the differences between each pixel are not significant enough to be observed by the human eye, the chromaticity of each pixel is slightly different. However, at normal emission, the chromaticity of each pixel is somewhat different; the observed color of the pixels from the device of

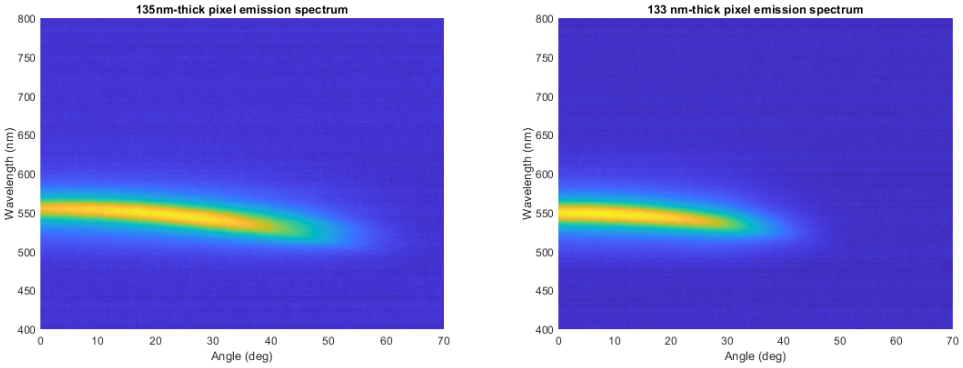

(a) (b)

Figure 3.6: ARES spectra from pixels with 135 (left) and 133 nm thickness (right).

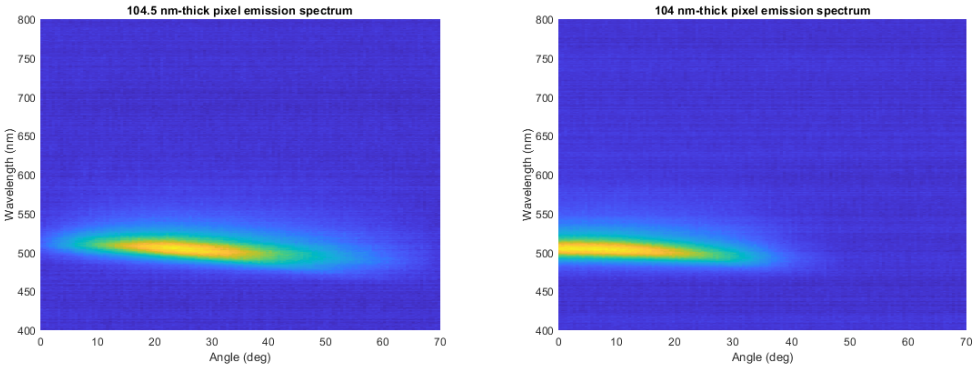

(a) (b)

Figure 3.7: ARES spectra from pixels with 104.5 (left) and 104 nm thickness (right).

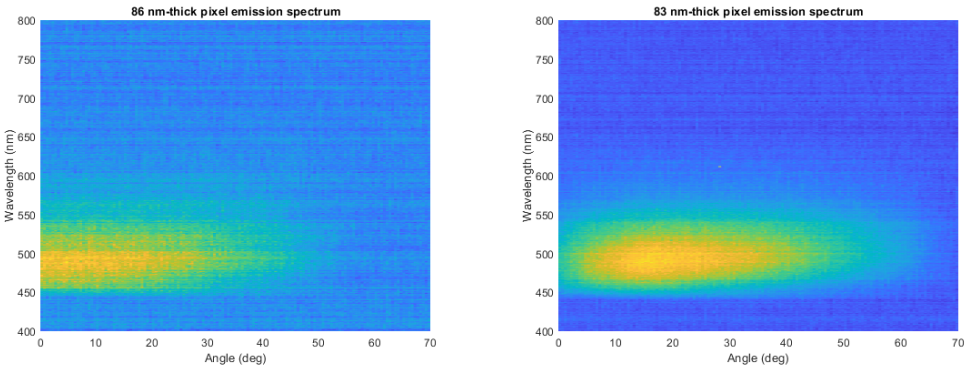

(a) (b)

Figure 3.8: ARES spectra from pixels with 86 (left) and 83 nm thickness (right), exhibiting no cavity effect. High background intensity comes from pixel crosstalk.

about 104 nm thickness moves closer to the green end of the chromaticity plot, and the pixels from the device with about 85 nm thickness become a lighter blue. While the fabricated devices do not span the entire visible spectrum, the difference in emission associated with their differences in thickness does result in different colored emissions in the blue and green portion of the visible spectrum.

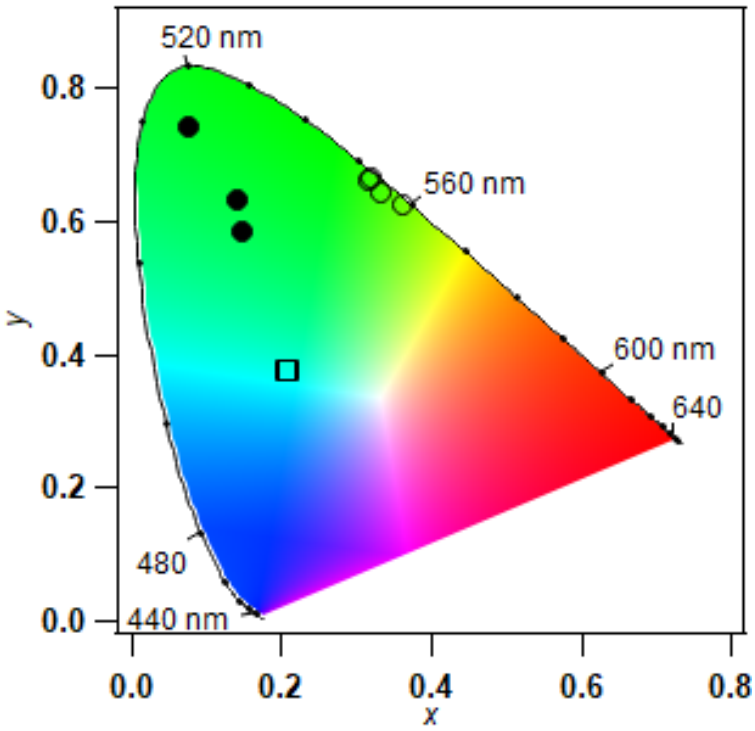

Figure 3.9: Chromaticity coordinates of fabricated devices at normal emission. The hollow squares, hollow circles, and filled circles represent the color of normal emission from ≈ 86 nm, ≈ 138 nm, and ≈ 104 nm pixels, respectively.

Chapter 4

Conclusion

This project's theoretical devices did span the color gamut of the visible spectrum, whereas the fabricated devices' emission was limited to one section of the spectrum. These results suggest that the experimental technique of depositing the thin films in a linear gradient is not very effective for the creating microcavity OLEDs for the purpose of drastically altering the emission spectra from one device's subpixels; however, the results confirm that changing device thickness does alter the emission spectra and color of emitted light.

There are several possibilities for future work. One possibility is producing ITO-based devices using the same experimental technique; while these devices would lack the cavity effect associated with microcavity-based devices, it is possible that the emission spectrum of each pixel would differ more significantly than seen in this project; this is because an ITO-based device's pixels often have more space between them compared to the pixels created by the fabrication process used here, which would involve a greater variation in optical medium thickness across each device.

Additionally, mircocavity-based devices fabricated using slightly different methods of creating variations in thickness could produce emission across a larger portion of the visible spectrum. For instance, a layer of constant thickness of each charge transport material could be deposited before depositing the same material without rotation to produce a thicker optical medium. Thermal evaporation across substrates with larger areas could also produce more significant variations in emitted color by incorporating greater variations in thickness across one device.

Acknowledgements

Matthew White supervised the project. David Allemeier developed the simulation tools. Experimental procedures were developed by Matthew White and Ekraj Dahal.

Appendix

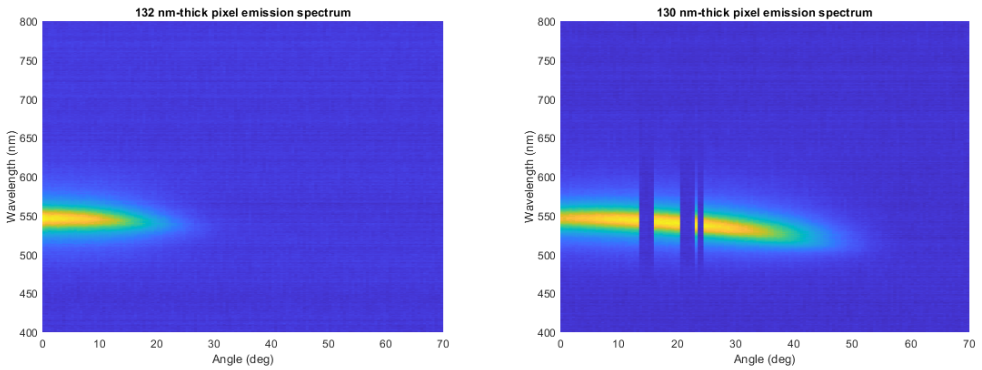

(a) (b)

Figure 4.1: ARES spectra from pixels with 132 (left) and 130 nm thickness (right). Electrical contact was briefly lost during measurements for 130 nm pixel.

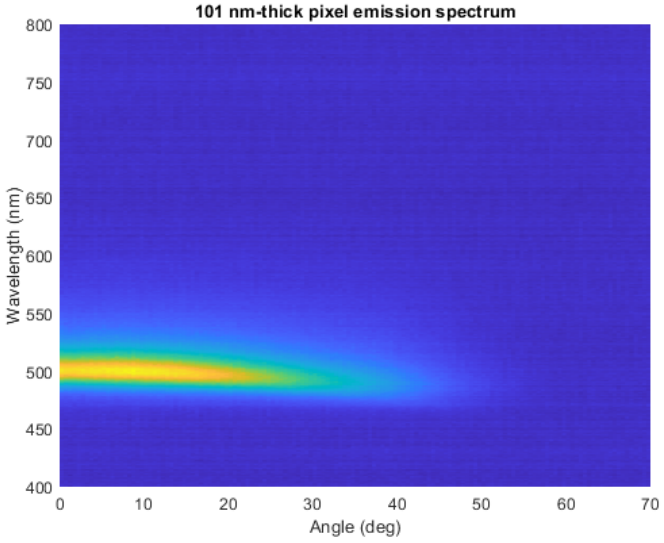

Figure 4.2: ARES spectrum from pixel with 101 nm thickness.

Bibliography

[1] S. Lim, D. Kang, O.A. Ogunseitan, and J.M. Schoenung. "Potential Environmental Impacts of Light-Emitting Diodes (LEDs): Metallic Resources, Toxicity, and Hazardous Waste Classification". In: *Environ. Sci. Technol* 45 (2011), pp. 320–327.

[2] R. Meerheim, Björn Lüssem, and Karl Leo. "Efficiency and Stability of p-i-n Type Organic Light Emitting Diodes for Display and Lighting Applications". In: *Proceedings of the IEEE* 97.9 (2009), pp. 1606–1626. DOI: https://doi.org/10.1109/JPROC.2009.2022418.

[3] B.Y. Jung, N.Y. Kim, C. Lee, C.K. Hwangbo, and C. Seoul. "Control of resonant wavelength from organic light-emitting materials by use of a Fabry–Perot microcavity structure". In: *Applied Optics* 14.6 (2002), pp. 3312–3318.

[4] D.P. Puzzo, H.G. Helander, P.G. O'Brien, Z. Wang, N. Soheilni, N. Kherani, Z. Lu, and G.A. Ozin. "Organic Light-Emitting Diode Microcavities from Transparent Conducting Metal Oxide Photonic Crystals". In: *Nano Letters* 11 (2011), pp. 1457–1462. DOI: dx.doi.org/10.1021/nl104036c.

[5] E. Dahal, D. Allemeier, B. Isenhart, K. Cianciulli, and M.S. White. "Characterization of higher harmonic modes in Fabry–Pérot microcavity organic light emitting diodes". 2021.

[6] T. Matsushima, G. Jin, and H. Murata. "Marked improvement in electroluminescence characteristics of organic light-emitting diodes using an ultrathin hole-injection layer of molybdenum oxide". In: *Applied Physics Letters* 104.054501 (2008). DOI: https://doi.org/10.1063/1.2974089.

[7] K.J. Bergemann, R. Krasny, and S.R. Forrest. "Thermal properties of organic light-emitting diodes". In: *Organic Electronics* 13 (2012), pp. 1565–1568.

[8] N. Takada, T. Tsutsui, and S. Saito. "Control of emission characteristics in organic thin-film electroluminescent diodes using an optical-microcavity structure". In: *Applied Physics Letters* 63.15 (1993), pp. 2032–2034. DOI: https://doi.org/10.1063/1.110582.

[9] A. Dodabalapur, L.J. Rothberg, T.M. Miller, and E.W. Kwock. "Microcavity effects in organic semiconductors". In: *Applied Physics Letters* 64 (1994), pp. 2486–2488. DOI: https://doi.org/10.1063/1.111606.

[10] B. Isenhart. "Precise Control of Organic LED Emission Through OpticallyResonant Microcavity Confinement". Undergraduate honors thesis. University of Vermont, 2019.

[11] A. Dodabalapur, L.J. Rothberg, R.H. Jordan, T.M. Miller, R.E. Slusher, and J.M. Phillips. "Physics and applications of organic microcavity light emitting diodes". In: *Journal of Applied Physics* 80.12 (1996), pp. 6954–6964. DOI: https://doi.org/10.1063/1.363768.

[12] R.E. Slusher. "Optical Microcavities in Condensed Matter Systems". In: *Solid State Communications* 92.1-2 (1994), pp. 149–158.

[13] P.N. Stavrinou, M. Whitehead, G. Parry, and C.C. Button. "Monolithic Integration of Multi-Color Organic LEDs by Grayscale Lithography". In: *Advanced Materials* 22 (2010), pp. 4634–4638. DOI: https://doi.org/10.1002/adma.201002033.

[14] G.H. Lodden and R.J. Holmes. "Polarization splitting in polariton electroluminescence from an organic semiconductor microcavity with metallic reflectors". In: *Applied Physics Letters* 98.233301 (2011).

[15] M. Shaw and M. Fairchild. "Evaluating the 1931 CIE Color-Matching Functions". In: *COLOR research and application* 27.5 (2002), pp. 316–329.

[16] T. Tsuzuki, N. Shirasawa, T. Suzuki, and S. Tokito. "Color Tunable Organic Light-Emitting Diodes using Pentafluorophenyl-Substituted Iridium Complexes". In: *Advanced Materials* 15.17 (2003), pp. 1455–1458. DOI: 10.1002/adma.200305034.

[17] E.S. Hellerich, E. Manna, R. Heise, R. Biswas, R. Shinar, and J. Shinar. "Deep blue/ultraviolet microcavity OLEDs based on solution-processed PVK:CBP blends". In: *Organic Electronics* 24 (2015), pp. 246–253. DOI: http://dx.doi.org/10.1016/j.orgel.2015.05.041.

[18] R. Liu, C. Xu, R. Biswas, J. Shinar, and R. Shinar. "MoO_3 as combined hole injection layer and tapered spacer in combinatorial multicolor microcavity organic light emitting diodes". In: *Applied Physics Letters* 99.093305 (2011). DOI: https://doi.org/10.1063/1.3623482.

[19] F.N. Ventsch, M.C. Gather, and K. Meerholz. "Towards organic light-emitting diode microdisplays with sub-pixel patterning". In: *Organic Electronics* 11 (2010), pp. 57–61.

[20] M.C. Gather, N.M. Kronenberg, and K. Meerholz. "Monolithic Integration of Multi-Color Organic LEDs by Grayscale Lithography". In: *Advanced Materials* 22 (2010), pp. 4634–4638. DOI: https://doi.org/10.1002/adma.201002033.

[21] B. Ruhstaller, T. Beierlein, H. Riel, S. Karg, J. C. Scott, and W. Riess. "Simulating Electronic and Optical Processes in Multilayer Organic Light-Emitting Devices". In: *IEEE Jornal of Selected Topics in Quantum Electronics* 9.3 (2003), pp. 723–730.

[22] T.J. Wang, C. Cao, and C. Wang. "On the developments and applications of optical microcavities: an overview". In: *Science China Information Sciences* 56.122401 (2013), pp. 1–15. DOI: 10.1007/s11432-013-5041-0.

[23] H. Benisty, R. Stanley, and M. Mayer. "Method of source terms for dipole emission modification in modes of arbitrary planar structures". In: *Journal of the Optical Society of America* 15.5 (1998), pp. 1192–1201.

[24] D. Yokoyama. "Molecular orientation in small-molecule organic light-emitting diodes". In: *Journal of Materials Chemistry* 21 (2011), pp. 19187–19202.